

# THE HYDROGEN EPOCH OF REIONIZATION ARRAY DISH: CHARACTERIZATION WITH ELECTROMAGNETIC SIMULATIONS

EWALL-WICE AARON<sup>1,2</sup>, ABRAHAM NEBEN<sup>1,2</sup>, NIPANJANA PATRA<sup>5</sup>, THYAGARAJAN NITHYANANDAN<sup>6</sup>, RICHARD BRADLEY<sup>3,4</sup>,  
 JACQUELINE HEWITT<sup>1,2</sup>, ALI S. ZAKI<sup>5</sup>, BOWMAN JUDD<sup>6</sup>, CHENG CARINA<sup>5</sup>, DEBOER DAVID<sup>5</sup>, PARSONS AARON<sup>5</sup>, VENTER  
 MARIET<sup>7</sup> AND OTHERS.

*Draft version November 9, 2015*

## ABSTRACT

Using electromagnetic simulations, we assess the spectral properties of the antenna element of the Hydrogen Epoch of Reionization Array (HERA) in order to both establish a specification for the degree of spectral structure that is permissible to sufficiently isolate foregrounds and allow a detection of the cosmological 21 cm signal and verify direct laboratory measurements of the dish characteristics. We find that our simulations are in good agreement with field measurements. Using simulations of foregrounds, we find that the  $\approx -40$  dB response at 60 ns of the HERA dish is sufficient to isolate the cosmological 21 cm signal  $\approx 0.2$  hMpc<sup>-1</sup> at  $z \approx 8.5$  and obtain a high signal to noise detection of the power spectrum. At its current state, the reflections of the HERA dish design do significantly impact its ability to constrain the  $R_{\text{mfp}}$  reionization parameter for a number of models since they prevent direct measurements of the “knee” feature. This study represents the first time that direct measurements a 21 cm interferometer design have been translated into its ability to constrain the physics of reionization.

## 1. INTRODUCTION

Observations of the redshift 21 cm radiation neutral hydrogen in the intergalactic medium (IGM) have the potential to illuminate the hitherto unobserved *dark ages* and *cosmic dawn*, revolutionizing our understanding of the first UV and X-ray sources in the universe and how their properties influenced galactic evolution (see Furlanetto et al. (2006), Morales & Wyithe (2010), and Pritchard & Loeb (2012) for reviews). As of now, two major experimental endeavors are underway to make a first detection of the 21 cm signal with most focusing on the Epoch of Reionization (EoR) in which UV photons from early galaxies transformed the hydrogen in the universe from neutral to ionized. The first involves measuring the sky-averaged global signal and is being pursued by experiments such as EDGES (Bowman & Rogers 2010), LEDA (Greenhill & Bernardi 2012), DARE (Burns et al. 2012), SciHi (Voytek et al. 2014), and BIGHORNS (Sokolowski et al. 2015) coming online in their planning stages or taking data. The second attempts to observe spatial fluctuations in the 21 cm emission using radio interferometers. As of now, a first generation of interferometry experiments are taking data in an attempt to make a first statistical detection of the power spectrum of 21 cm brightness temperature fluctuations. These include the Giant Metrewave Telescope (GMRT) (Paciga et al. 2013), the Low Frequency ARray (LOFAR), (van Haarlem et al. 2013), the Murchison Widefield Array (?) and the Precision Array for Probing the Epoch of Reionization (PAPER) (Parsons et al. 2010).

The primary obstacle to obtaining a high redshift detection of the cosmological signal through both of these methods is the existence of foregrounds that are  $\sim 10^5 - 10^6$  times brighter. While requiring much greater sensitivity to global-signal experiments, interferometers have the advantage that these spectrally smooth foregrounds naturally avoid a significant region of  $k$ -space, known as the *EoR window*, occupying a region known as the *wedge* (Datta et al. 2010; Vedantham et al. 2012; Parsons et al. 2012; Thyagarajan et al. 2013; Liu et al. 2014a,b), however any structure in the frequency response of the instrument has the potential to leak foregrounds into the EoR window, masking our signal. Indeed, low level spectral structures in the analogue and digital signal chains on the initial buildout of the MWA are proving to be a significant obstacle (Dillon et al. 2015; Ewall-Wice et al. submitted 2015; Beardsley et al. in preparation).

While, in principle, spectral structure in the bandpass of the instrument may be removed in calibration, simulations show that any mismodeling of emission and the primary beam, potentially below the confusion limit, will mix the significant spectral structure on long baselines into short ones, masking the signal entirely (Barry et al. in preparation). While redundant calibration (Wieringa 1992; Liu & Tegmark 2011; Zheng et al. 2014) is able to calibrate the independent of a detailed model of the sky, any direction-dependent chromatic structure in the primary beam of the instrument introduces additional degrees of freedom that must be modeled, potentially leading to signal loss and the introduction of spurious spectral structure due to unmodeled foregrounds in long baselines. Because of our limited knowledge of foregrounds at low-frequency and the fidelity of calibration algorithms, the only sure way of building an instrument that will guarantee a detection of the redshifted 21 cm emission is to design it such that all spectral structure in the signal chain is limited to a finite region of delay space, well below the wedge.

<sup>1</sup> MIT Kavli Institute for Cosmological Physics

<sup>2</sup> MIT Dept. of Physics

<sup>3</sup> National Radio Astronomy Obs., Charlottesville VA

<sup>4</sup> Dept. of Astronomy, U. Virginia, Charlottesville VA

<sup>5</sup> Astronomy Dept. U. California, Berkeley CA

<sup>6</sup> School of Earth and Space Exploration, Arizona State U., Tempe AZ

The Hydrogen Epoch of Reionization Array (HERA) is an instrument currently taking first observations in the Karoo in South Africa with the ultimate goal of detecting the power spectrum of 21 cm brightness temperature fluctuations at high signal-to-noise (SNR) (Pober et al. 2014). A central principle in HERA's design is that it be calibration fail-safe such that a detection of the signal is guaranteed, even if the chromaticity of the instrument is not calibrated out. This paper and its companions (Neben et al. submitted; Patra et al. submitted; Thyagarajan et al. submitted) describe a multifaceted approach to establishing a stringent specification on the spectral structure permissible for HERA to be calibration fail-safe and determine to what extent its design meets these requirements. We accomplish this by establishing a spec with simulations of foregrounds (?) and verifying that HERA primary antenna element meets this spec with reflectometry (Patra et al. submitted) and Orbcomm beam mapping (Neben et al. submitted). These measurements are verified with detailed electromagnetic simulations which we describe in this work.

This paper is organized as follows. In § 2 we lay out our analytic framework for describing the impact of reflections and spectral structure on foreground leakage in delay-transform power spectra. In § 3 we describe our electromagnetic simulations of the HERA dish element. In § 4 we compare our simulation results to direct measurements of the primary dish element and in § ?? we apply our electromagnetic simulation results to simulations of foregrounds to determine the extent that the HERA dish's chromatic structure pollutes the EoR window and their impact on HERA's overall sensitivity. We conclude in § 6.

## 2. THE IMPACT OF REFLECTIONS ON DELAY-TRANSFORM POWER SPECTRA

In this section, we show how reflections in the analogue signal path of an antenna lead to foreground contamination of the EoR window. Intuitively, any reflections in the signal path introduce sinusoidal ripples in the frequency dependent gain of the instrument. Since reflection delay is the Fourier dual to frequency, reflections at larger delays introduce ripples at higher frequencies. Isolation of the 21 cm signal from foregrounds that are over five orders of magnitude brighter depends critically on the fact that their smoothness. Any sinusoidal frequency structure, introduced by the antenna gain will cause these foregrounds to mimic and swamp the signal unless they are brought below a level similar to the ratio between the foregrounds and the signal itself. We now derive this process in formal detail. A simple equation for effect of direction independent reflections in the signal chain of an interferometer, downstream of the receiver, has been derived in (Ewall-Wice et al. submitted 2015), we extend this analysis in this section by considering the direction dependent reflections that can occur within the antenna element. We assume that the intensity field on the sky is given by

$$I(\hat{\mathbf{k}}, f) \delta_D(\hat{\mathbf{k}} - \hat{\mathbf{k}}') = \langle s(\hat{\mathbf{k}}, f) s^*(\hat{\mathbf{k}}', f) \rangle_t^2 \quad (1)$$

where  $\delta_D$  is the Dirac delta function and  $\langle \rangle_t$  indicates an average in time. We imagine that the electric field as a function of time,  $\tilde{s}(\hat{\mathbf{k}}, t)$  arrives at an arbitrary origin at time  $t$  and at the various  $i^{th}$  antenna elements of an interferometer at locations  $\mathbf{x}_i$  at times  $\tau_i = \mathbf{x}_i \cdot \hat{\mathbf{k}}/c$ . We now consider reflections within a single dish element described by a direction dependent reflection coefficient<sup>7</sup>,  $\tilde{r}_i(\hat{\mathbf{k}}, \tau)$ , which re-introduce the signal at later times  $\tau$ . The voltage signal measured at the  $i^{th}$  antenna element,  $\tilde{v}_i$ , is the integral over solid angle of the convolution of the electric field entering the antenna (delayed by  $\tau_i$ ) with  $r_i(\hat{\mathbf{k}}, \tau')$ .

$$\tilde{v}_i(t) = \int d\Omega \int d\tau \tilde{r}_i(\hat{\mathbf{k}}, \tau) \tilde{s}(\hat{\mathbf{k}}, t - \tau_i - \tau) \quad (2)$$

An FX (or XF) correlator measures the time-averaged product of the fourier transform of the voltage streams between the  $i^{th}$  and  $j^{th}$  antenna. Fourier transforming the voltage stream from the  $i^{th}$  antenna we obtain

$$v_i(f) = \int d\Omega \int d\tau \tilde{r}_i(\hat{\mathbf{k}}, \tau) s(\hat{\mathbf{k}}, f) e^{-2\pi i f(\tau_i + \tau)} \quad (3)$$

The time averaged product between the two antennas is

$$V'_{ij}(f) = \langle v_i(f) v_j^*(f) \rangle_t = \int d\Omega \int d\tau \tilde{r}_i(\tau) d\tau' \tilde{r}_j^*(\tau') e^{-2\pi i f(\tau - \tau')} I(\hat{\mathbf{k}}, f) e^{-2\pi i \Delta\tau_{ij} f} \quad (4)$$

where  $\Delta\tau_{ij} = \tau_i - \tau_j = (\mathbf{x}_i - \mathbf{x}_j) \cdot \hat{\mathbf{k}}/c$ . We eliminated one of the solid angle integrals using equation 1.

Defining  $\mathbf{u}_{ij} = f(\mathbf{x}_i - \mathbf{x}_j)/c$ , we obtain,

Then the resulting visibilities obtained by cross correlating antenna  $i$  and antenna  $j$  are given by

$$V'_{ij}(f) = \int d\Omega r_i(\hat{\mathbf{k}}, f) r_j^*(\hat{\mathbf{k}}, f) I(f, \hat{\mathbf{s}}) e^{2\pi i f \mathbf{u}_{ij} \cdot \hat{\mathbf{k}}/c}, \quad (5)$$

where  $\mathbf{b}_{ij} = (\mathbf{x}_i - \mathbf{x}_j)$  to use the usual  $uv$  notation of interferometry.  $r_i(\hat{\mathbf{k}}, f)$  is the inverse fourier transform of the reflection response of the dish, hence we see that the reflection response is precisely the Fourier dual to the Dish's frequency domain voltage beam. Setting a specification on reflections is hence equivalent to setting a specification on the spectral smoothness of the voltage beam.

<sup>7</sup> Ignoring reflections between multiple dish elements which we treat in Appendix A

In order to separate spectrally smooth foregrounds from our signal, we expect to use the *delay transform* over frequency, defined as (Parsons et al. 2012)

$$\tilde{V}_{ij}(\tau) = \int df e^{2\pi i \tau f} V_{ij}(f) \quad (6)$$

Applying this to equation 5, we obtain

$$\tilde{V}'_{ij}(\tau) = \int d\Omega \int df r_i(\hat{\mathbf{k}}, f) r_j^*(\hat{\mathbf{k}}, f) I(f, \hat{\mathbf{k}}) e^{2\pi i f (\mathbf{b}_{ij} \cdot \hat{\mathbf{k}} / c - \tau)} \quad (7)$$

Let's examine the quantity within the angular integral. For each  $\hat{\mathbf{k}}$ , we see that each source is mapped to a line  $\tau = \mathbf{b}_{ij} \cdot \hat{\mathbf{k}} / c$ , resulting in the much discussed “wedge” (Datta et al. 2010; Vedantham et al. 2012; Parsons et al. 2012; Thyagarajan et al. 2013; Liu et al. 2014a,b). The presence of the frequency dependent beam causes each source line to be convolved in delay with the direction dependent kernel

$$\tilde{R}_{ij}(\hat{\mathbf{k}}, \tau) = \int d\tau' \tilde{r}_i(\hat{\mathbf{k}}, \tau - \Delta\tau) \tilde{r}_j^*(\hat{\mathbf{k}}, -\Delta\tau). \quad (8)$$

which is the convolution of the delay response of voltage beam  $i$  with the complex conjugate of voltage beam  $j$  evaluated on a negative  $\tau$ -axis,  $\tilde{r}_i(\hat{\mathbf{k}}, \tau), \tilde{r}_j^*(\hat{\mathbf{k}}, \tau)$ . Note that this is not equal to the convolution of the voltage response with its complex conjugate, which would lead to foreground power only being bled out to positive delays. Usually, beams have a different delay structure in each direction, and we demonstrate the effect of foreground smearing in Fig. 1 for a simple model with only three sources. Without reflections, the sources would form lines in  $b - \tau$  space. With the reflections, the sources are smeared out, leading to supra-horizon emission. For the sake of pedagogy, we now consider the case

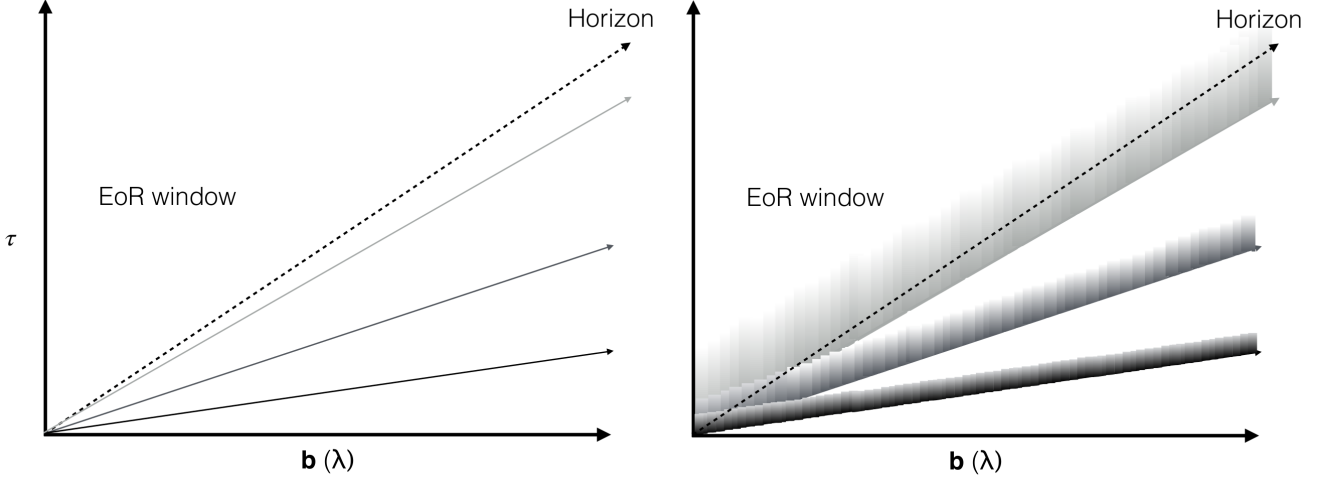


FIG. 1.— We demonstrate the impact on foregrounds of the frequency dependent beam. Left: The location of three sources in delay space assuming a frequency independent beam (no reflections in the antenna element). Right: the presence of chromaticity due to reflections in the antenna smears the source in delay with the kernel given by equation 8. Since the frequency response of the dish is a function of direction on the sky, the shape of the delay kernel is different for each source line. We see that this smearing can lead to substantial supra-horizon emission. Sources near zenith (low delay) tend to have a larger maximum since the beam gain is larger near zenith, but a more compact kernel (since beam bore-sights tend to have less spectral structure). Meanwhile, sources near the horizon have a much smaller maxima but have less compact kernels.

where the beam can be factored into angular and frequency dependent components,  $r_i(\hat{\mathbf{k}}, f) = g_i(f) a_i(\hat{\mathbf{k}})$ . For such a case, every line in Fig. 1 would be convolved with the same delay dependent shape, normalized to the gain of  $a_i(\hat{\mathbf{k}})$ . In this case, we have

$$\tilde{V}'_{ij}(\tau) = \int d\tau' \int d\tau'' \tilde{g}_i(\tau' - \tau'') \tilde{g}_j^*(\tau'') \tilde{V}_{ij}(\tau - \tau') \quad (9)$$

We can further simplify matters by assuming that  $\tilde{g}_i(\tau = 0) \gg \tilde{g}_i(\tau > 0)$ , which is often a good assumption at large delays for the relatively smooth bandpasses our instruments are designed to have.

$$\tilde{V}'_{ij}(\tau) \approx \tilde{g}_i(0) \int d\tau' \tilde{g}_j^*(\tau') \tilde{V}_{ij}(\tau - \tau') + \tilde{g}_j^*(0) \int d\tau' \tilde{g}_i(\tau') \tilde{V}_{ij}(\tau - \tau') \quad (10)$$

Hence, to first order, the impact of reflections is to convolve the delay-transformed visibility with the voltage beam of the instrument, which acts as the power-kernel. This may be a somewhat un-intuitive result since we might naively

## 3.1. The Simulations

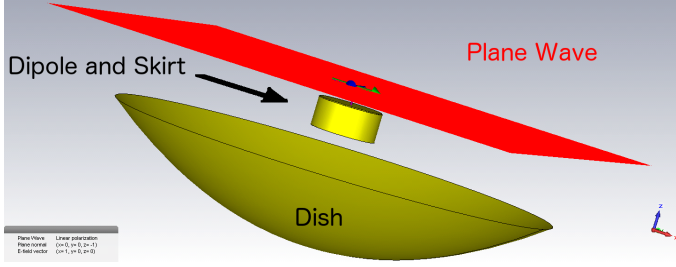


FIG. 2.— A rendering of our time domain simulation at  $t = 0$ , demonstrating the geometry and setup of our electromagnetic simulation. The plane wave is started just above the feed (red plane).

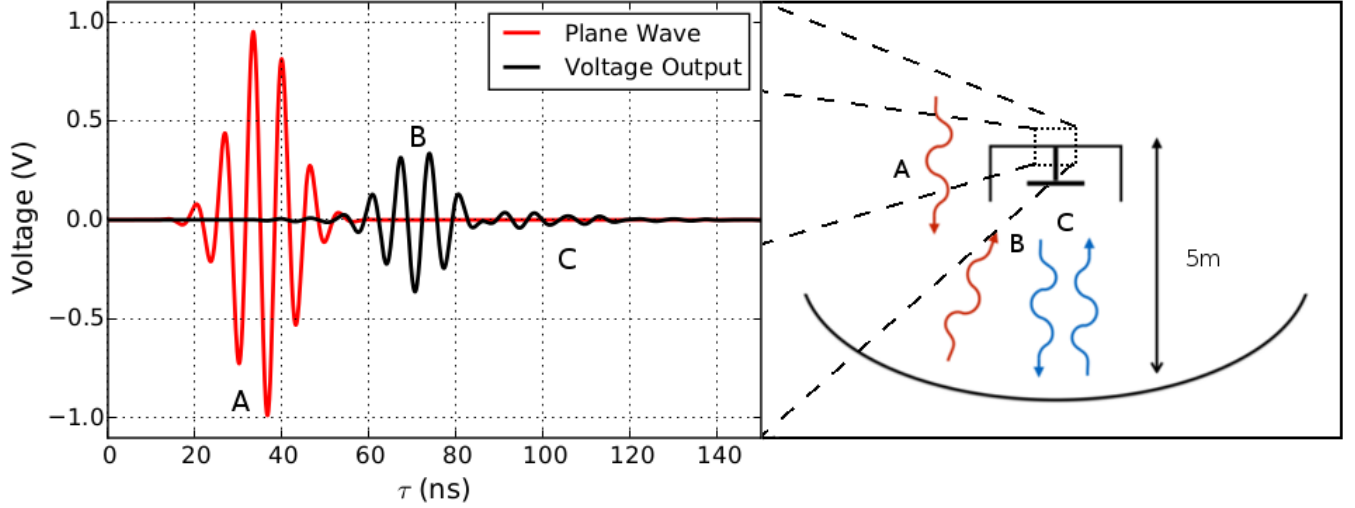


FIG. 3.— An illustration of our simulation products and their origin in the HERA antenna geometry. A plane wave is injected from above the feed (red line). The amplitude of the electric field of the plane wave at output of the feed along with the voltage at the feed terminal outputs is recorded (black line). The feed in our simulation is situated 5 m above the bottom of the dish, hence there is a  $\approx 30$  ns delay between when the plane wave passes the terminal for the first time (A) and when it is first absorbed in the dipole (B), leading to the voltage response. Of concern to 21 cm experiments are the subsequent reflections between the feed and the dish (C) which can lead to large delay contamination of the EoR window.

expect for the power-kernel to be the square of the delay-response. This linear falloff puts exquisite requirements on the smoothness of the beam, requiring that it fall roughly six orders of magnitude in delay before the signal is accessible.

In this paper, we derive  $\tilde{r}_i(\mathbf{k}, \Delta\tau)$  for the HERA antenna element using electromagnetic simulations, in order to verify direct measurements of the antenna element with refelctometry (Patra et al. submitted) and Orbcomm measurements of the beam (Neben et al. submitted). We also explore the implications of the HERA dish's  $\tilde{r}_i(\mathbf{k}, \tau)$  on the scientific bottom line for EoR, using the Fisher Matrix Formalism.

## 3. ELECTROMAGNETIC SIMULATIONS OF THE HERA DISH ELEMENT

In Fig. 2 we show the geometry of the electromagnetic simulation. **Rich: fill in the details here**

## 3.2. Deconvolving the Response Function

Since our simulation is sampled in finite time steps, we will adopt discretized notation for this section. In particular, our simulation consists of  $N$  samples, evenly spaced by  $d\tau$  at times  $\tau_n = n \times d\tau$ . In our simulation, we obtain the voltage at the feed output at time  $\tau_n$  which we will call  $\tilde{v}_n$ . It is related to the input plane wave through the discrete convolution

$$\tilde{v}_n(\mathbf{k}) = \sum_m \tilde{r}_m(\mathbf{k}) \tilde{s}_{n-m}(\mathbf{k}), \quad (11)$$

We may undo this convolution by taking a discrete Fourier transform (DFT) of both  $\tilde{\mathbf{v}}$  and  $\tilde{\mathbf{s}}$  in time, dividing them in Fourier space, and taking an inverse DFT back. Symbolically,

$$\tilde{\mathbf{r}}(\mathbf{k}) = \mathcal{F}^{-1} \left[ \frac{\mathcal{F}\tilde{\mathbf{v}}(\mathbf{k})}{\tilde{\mathbf{s}}(\mathbf{k})} \right] \quad (12)$$

where  $\mathcal{F}$  is the Fourier transform matrix for a 1d vector of length  $N$ .

$$\mathcal{F}_{mn} = e^{2\pi i mn/N} \quad (13)$$

In Fig. 4 we show the amplitude of the Fourier transform of our Gaussian input, centered at 150 MHz along with the voltage response. Since our input is band limited between  $\approx 20$  and 280 MHz, the direct ratio of our voltage response and input wave is dominated by numerical noise outside of this range. We eliminate these numerical artifacts by multiplying our ratio by a Hamming window between 50 MHz and 250 MHz and set our estimate to zero elsewhere. From a physical standpoint, this is sensible since 21 cm experiments only observe a limited bandwidth. PAPER's correlator, which will initially serve as the HERA backend samples over a 100 MHz instantaneous frequency interval. Hence analogue filtering is applied to limit the incoming signal within a finite bandwidth and prevent aliasing.

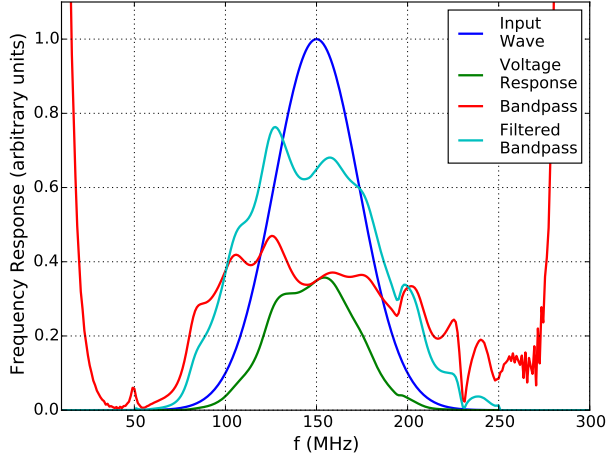


FIG. 4.— The absolute value of the discrete Fourier transform of our simulation outputs. We obtain the effective response function of the dish by Fourier transforming the voltage output from our dish (green line) and dividing by the Fourier transform of the input wave (blue line). The simple ratio is plotted as a red line. Since our input is limited to frequencies between  $\approx 20$  and 280 MHz, there is significant numerical noise that will effect our result outside of this region which we see in the divergene of the red line towards the edges of the plot. To eliminate this noise, we multiply by a Hamming window between 50 and 250 MHz and set our estimate to zero elsewhere. The Fourier transform of our response estimate with the filter applied is shown as a cyan line.

### 3.3. Extrapolating the Bandpass and Power Kernel

Our deconvolution gives us the time-domain voltage response of the HERA antenna element. We plot the absolute value of this response in Fig. 5, seeing that it drops to  $-20$  dB after  $\approx 75$  ns. The power-kernel that convolves visibilities to higher delays is the convolution of  $\tilde{r}(\tau)$  with its complex conjugate, which we plot as the red line. The convolution is in very good agreement with the voltage response itself which is explained by the fact that second order terms of the convolution, approximately given by  $|\tilde{r}(\tau)|^2$  (green line) are over two orders of magnitude smaller above 50 ns.

Our simulations of the Dish response only extend to  $\approx 300$  ns, however, we wish to understand the impact of reflections on the frequency dependent gain of an interferometer like HERA, which has a spectral resolution of 100 kHz. Obtaining such frequency resolution would require a calculation of the voltage response out to  $100 \mu\text{s}$ , over two orders of magnitude beyond the time limit of our current simulation. Fortunately, there exists a way of extrapolating our results which is highly physically motivated. We first note that  $\tilde{r}(\tau)$  exhibits a pivot at around 75 ns, falling rapidly for the first  $\sim 60$  ns or so before leveling out and following a much shallower trend that is characterized by periodic lobed structures every  $\approx 30$  ns. The initial falloff is likely the intrinsic response of the feed element itself, caused by residual currents that were excited by the incident wave. The scalloped structures that dominate the slower, long-term fall-off is almost certainly caused by reflections between the feed element and the vertex of the dish. This is due to the fact that the round-trip delay between the feed and the dish, 5 m below, is  $\approx 30$  ns. This long term falloff is precisely what we must model in order to extrapolate to the very long delays required to model 100 kHz structures and the reflections provide us with a simple physical model for doing so. Adopting the notation of (Patra et al. submitted), we let  $\Gamma_d$  represent the reflection coefficient of the Dish vertex and  $\Gamma_f$  represent the reflection coefficient of the feed. An electromagnetic wave incident on the feed, at  $t = 0$ , is accepted with amplitude  $(1 - \Gamma_f)$ . The reflected component travels back to the dish and acquires an amplitude of  $(\Gamma_f \Gamma_d)$  before returning at time,  $\tau_d$  later where  $(1 - \Gamma_f)$  will be accepted and so forth. The time dependent voltage at the feed from these reflections is thus

$$\tilde{v}_r(t) = \sum_m (\Gamma_f \Gamma_d)^m \tilde{s}(t - m\tau_d) \quad (14)$$

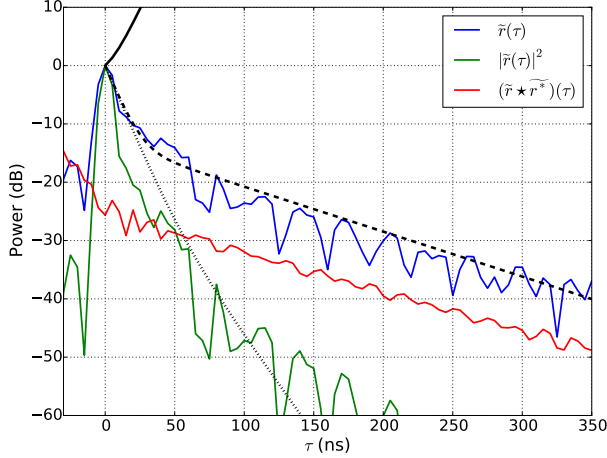


FIG. 5.— Our estimate of  $\tilde{r}(\tau, \theta = 0)$ , the voltage response of the HERA dish at zenith (blue line) along with its square (green line) which falls off significantly faster with delay. The power kernel for identical dishes,  $\tilde{r} \star \tilde{r}^*$ , the voltage response convolved with itself, is plotted with a red line. Because the  $\tau = 0$  response of the dish is significantly larger than the reflections, linear terms in the convolution dominate the squared terms whose magnitude roughly corresponds to the green line. Hence, the power kernel is well approximated by  $\tilde{r}$  itself, verifying our result in equation 10. We fit a double power law model to both the power kernel (solid black line) and the voltage response (dashed black line) and find that it is a good approximation for the long-time scale behavior of both. We also plot the falloff of reflections with  $Y = 0.1$  in equation ?? which is representative of the measured and simulated reflection coefficient of the feed to waves at zenith. The observed reflections are significantly worse.

Hence

$$\tilde{r}_r(\tau) = \sum_m (\Gamma_f \Gamma_d)^m \delta_D(\tau - m\tau_d) \quad (15)$$

Since the number of reflections,  $m = t/\tau_d$ , than we can write the long-term delay response in discrete form as

$$\tilde{r}_n \approx (\Gamma_f \Gamma_d)^{nd\tau/\tau_d} \quad (16)$$

which is a power law. We thus model our discrete voltage response as a sum of two power laws, one to describe the rapid falloff at small delays from residual currents in the feed, and another at large delay to describe the reflections in the dish.

$$\tilde{r} = AX^{(\tau/30\text{ns})} + (1 - A)Y^{(\tau/30\text{ns})} \quad (17)$$

Strictly speaking, this equation is not correct in that it contains non-existent reflections at very small delays, however since the amplitude of these reflections is only several %, the formula is still accurate here. We fit our voltage response function and power-kernel to this function, finding a best fit model for the voltage kernel of  $A \approx 0.95$ ,  $X \approx 0.18$ , and  $Y \approx 0.58$ . The large  $Y$  is unrepresentative of the feed reflection coefficient which has been simulated and measured to be  $\approx 0.1$  for a head-on EM wave, suggesting that the reflections are arriving from the sides and potentially involve only a small component of the dish and feed. Plotting the die off for the feed reflection coefficient yields dramatically better performance than what is measured. If the reflections are indeed originating from the sides, and a small component of the dish and feed arrangement, further suppression may be achieved through modifying this component.

#### 4. COMPARISON TO REFLECTOMETRY DATA

##### 4.1. The Delay Response at Zenith

In Fig. 6, we show the filtered response function deconvolved from our electromagnetic simulations. The response of the dish rapidly dies off as a function of time. After  $\approx 90$  ns, we observe lobed structures with a period of  $\approx 30$  ns which corresponds to the geometrical delay between the feed and the dish apex, indicating that the large  $\tau$  roll off is dominated by reflections between the feed and the dish.

Our simulations are intended to verify direct reflectometry measurements taken on a prototype of the HERA feed and dish in Green Bank, presented in (Patra et al. submitted). For the readers convenience, we briefly explain the reflectometry measurement here before comparing them to our simulation.

In the reflectometry measurement, a signal is sent from a Vector Network Analyzer (VNA) via a coaxial cable (which is calibrated out) into the back of the feed. The VNA then measures the ratio between returned and transmitted power as a function of frequency,  $S_{11}(f)$ . A fundamental difference between the reflectometry measurement and the delay response that we are attempting to obtain is that at zero delay,  $S_{11}$  is measuring the reflection of the input wave off of the back of the feed while in the delay response of the antenna, the zero delay reflection is the fraction of the electromagnetic wave off of the sky that is accepted by the feed. To obtain  $\hat{\rho}$ , we must correct for this difference.

It is shown in (Patra et al. submitted) that the correction is

$$\hat{\rho}(f) = \frac{\Gamma_a(f)}{1 - \Gamma_a(f)} [S_{11}(f) - \Gamma_a(f)] + 1 - \Gamma_a(f). \quad (18)$$

Applying this transformation to  $S_{11}(f)$  and taking a DFT into the time domain over a band of 100 – 200 MHz, we obtain a measurement based estimate of the dish response function at zenith which is plotted in Fig. 6 alongside our simulation result. The general trends of the two lines are in excellent agreement though the phases of the reflections at large time scales are  $\approx 10$  ns out of phase. As the long term delay structure of the delay response determines to what extent foregrounds leak out of the wedge, our simulations verify our measurement of the HERA dish’s key performance feature.

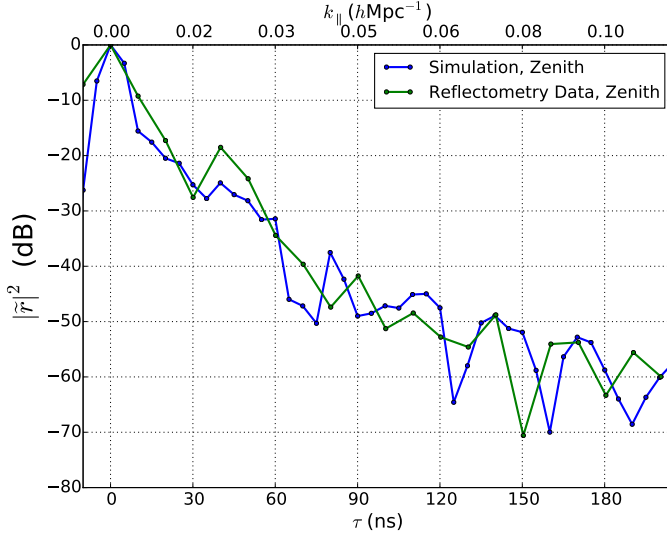


FIG. 6.— The response function deconvolved from our simulation (blue line) compared to the response function estimated from reflectometry measurements described in (Patra et al. submitted). Our simulations are in good agreement with the reflectometry results, dropping below  $-60$  dB at 180 ns. Since the foregrounds are  $\approx 10^6$  times larger than the signal, the necessary attenuation of zenith emission is obtained after  $\approx 0.1$   $h\text{Mpc}^{-1}$ .

#### 4.2. The Delay Response of the Sidelobes

After observing decent agreement between simulations and data, we now use our time-domain simulations to probe the side-lobe structure of the dish which are currently inaccessible to our experimental setup. Understanding the delay structure of the sidelobes is critical for several reasons. First, the sidelobes represent the largest delays occupied by foregrounds, hence the closest to the EoR window which we wish to keep foreground-free. While spectral leakage of sources at zenith may place them somewhere within the wedge, any spectral structure in the sidelobes is guaranteed to place these sources directly inside of the window. Second, the forshortening of diffuse structure near the horizon due to wide-field projection effects leads to a significant amount of foreground power entering at these delays, generally making them the most contaminated region of the wedge outside of the central lobe and leading to the so called “pitchfork” (Thyagarajan et al. 2015b,a).

We first attempt to explore the Dish sidelobe structure by running high resolution spatial beam maps **Rich fill in details of running 2D beam simulations**. However, comparison between individual frequency channels in both CST and FEKO indicates numerical precision errors **Show a figure of an attempted beam and frequency artifacts at zenith**.

Rather, we employ CST’s time domain mode to simulate the response of the dish to plane waves incident off of zenith to understand the frequency dependence of the side-lobes using the same technique that was described in § 3.2. In Fig. ??, we show the delay structure of the sidelobe response functions we obtain on a N-S line  $20^\circ$  and  $30^\circ$  from zenith, which approximately corresponds to the first two nulls of the beam. Each response is normalized to the voltage response at zero delay and zenith. We see that at zero delay, the sidelobes are  $\approx 20 - 25$  dB down. However, at larger delays,  $\approx 100$  ns, the difference with the  $20^\circ$  sidelobe is only  $\approx 5 - 10$  dB while the  $30^\circ$  sidelobe maintains  $\approx 15 - 20$  dB separation with the zenith response. This behavior indicates that while the overall amplitude of the sidelobes is reduced at zero-delay, the enhanced frequency structure over the sidelobes can mitigate this advantage at high delays, leading for the brightness of sidelobe foregrounds, leaked at  $\gtrsim 100$  ns to appear just as bright as the leakage of foregrounds from zenith at  $\gtrsim 100$  ns.

### 5. THE EFFECT OF THE HERA DISH CHROMATICITY ON FOREGROUND LEAKAGE AND SENSITIVITY



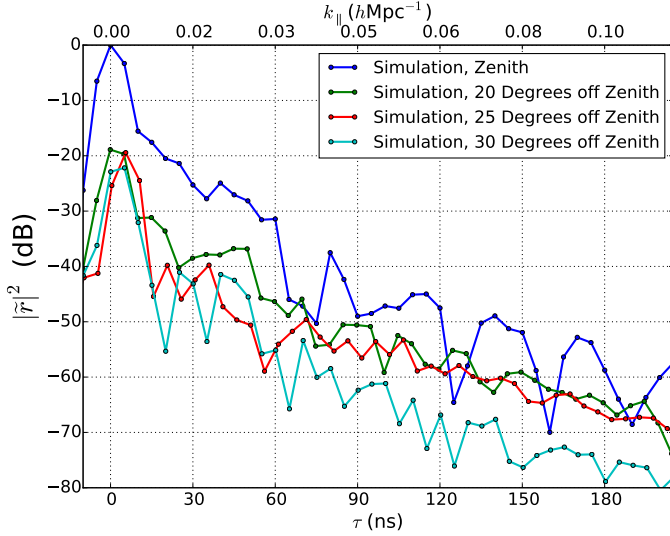


FIG. 7.— The modulus square of the voltage responses of the HERA dish to plane waves incident from zenith (blue line) along with  $20^\circ$ ,  $25^\circ$ , and  $30^\circ$  off-zenith along the NS line. While the sidelobes are suppressed to  $\approx 20 - 25$  dB at zero delay, they come within 5 dB of the zenith response at longer delays which can lead to the level of leakage for a source in the sidelobes being comparable to the leakage of a source from zenith. The fact that the sidelobes occupy a much larger solid angle with only moderate suppression at  $\sim 100$  ns coupled with their proximity to the horizon, suggests that they will dominate supra-horizon emission.

Having a thorough understanding of how the chromatic beam of the HERA dish leaks foregrounds into higher delays and a decent picture of the relevant voltage response of the dish itself, we are now in a position to explore the impact of the Dish's performance on the leakage of foregrounds beyond the wedge, and into the EoR window. Beyond the delay kernels considered in this paper and (Patra et al. submitted), the extent of leakage will depend both on the angular structure of the primary beam, which is established in (Neben et al. submitted) and the model of the foregrounds themselves. In this section, we investigate the amplitude of foreground leakage as a function of delay given an angular primary beam model and two models of the delay structure of the dish: one in which the frequency structure is constant in all directions, and another in which we take into account the increased spectral structure that we observed in § ??.

### 5.1. Simulating Foreground Visibilities with the Spectral Structure of the HERA Dish.

#### 5.2. How Deep Can we Clean?

The level of foreground subtraction possible depends on the number of time steps and redundant baselines that are averaged before performing the cleaning step. The standard deviation on the real and imaginary part of a single delay transformed visibility is given by (Morales & Hewitt 2004)

$$\Delta V = \frac{\sqrt{2B}k_B T_{sys}}{A_e \sqrt{\tau}} \quad (19)$$

where  $A_e$  is the effective area of the dish,  $B$  is the bandwidth,  $T_{sys}$  is the system temperature,  $\tau$  is the integration time, and  $k_B$  is the Boltzmann constant. The system temperature can be calculated by assuming that  $T_{sys} = 100\text{K} + T_{sky}$  where 100 K is the temperature of the PAPER receiver and  $T_{sky} = 60(\lambda/1\text{meter})^{2.55}$  is the sky temperature (?). For  $A_e$  we use the value of 75 m determined in (Neben et al. submitted). If we assume that each baseline is cleaned independently and that the integration time is  $\tau \approx 60\text{s}$ , then the noise level at 150 MHz is approximately 9.9 Jy MHz. In order to avoid subtracting noise, we assume that cleaning is performed down to  $5\sigma$ . In Fig. 8, we see that cleaning to  $5\sigma$

#### 5.3. The Impact of Delay-Rate Filtering.

#### 5.4. The Implications of Dish Reflections on EoR Science

Since the amplitude of the 21 cm signal is maximal at smaller  $k$  values, a loss of large scale signal out to  $0.25 h\text{Mpc}^{-1}$  will eliminate some of the power spectrum modes that HERA will have the greatest SNR on, impacting our overall sensitivity. We address the change in SNR and its implications on HERA's ability to place constraints on reionization parameters in this section, using the Fisher Matrix Formalism.

## 6. CONCLUSIONS

## REFERENCES



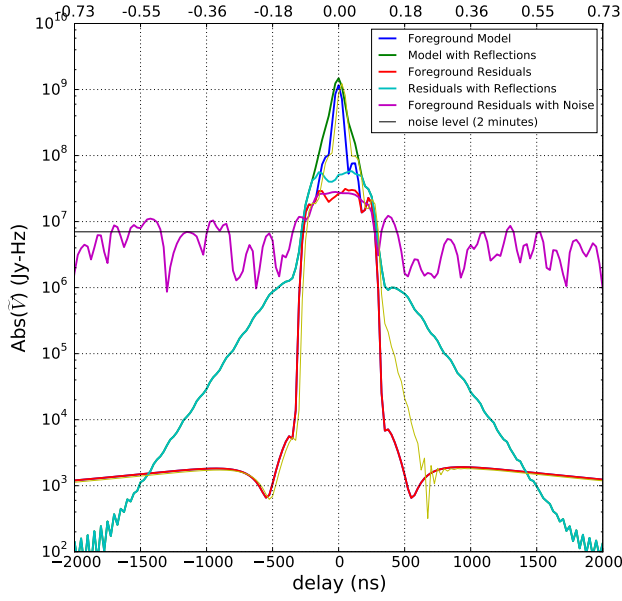


FIG. 8.— The absolute magnitude of a delay transformed 14-meter baseline (blue line) compared to the same visibility (green line) contaminated by reflections at the level observed in the HERA dish design. We see that the extended delay kernel smooths out structure, originating from foregrounds, within the horizon. For HERA, we expect to use the delay-clean to remove foregrounds. However, the depth of cleaning is limited by the noise level on a single baseline (black line). We show the foreground residuals with arising from a clean down to the  $5\sigma$  noise level after 2 minutes of integration, seeing that cleaning at this cadence achieves  $\approx$  two orders of magnitude of foreground reduction. The reflections in the dish lead to extensive winged structures that bleed into the EoR window and are well below the thermal noise level. All data in this plot are obtained from a 100 MHz bandwidth centered at 150 MHz.

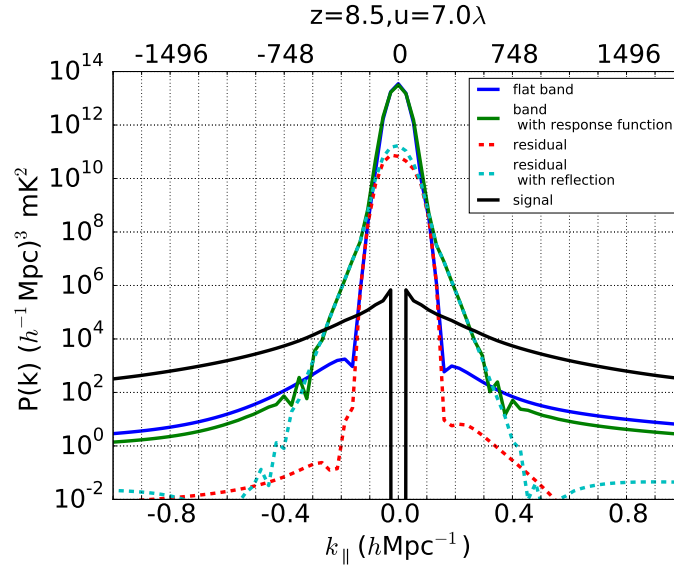


FIG. 9.— The delay transformed power spectra of foregrounds with (blue line) and without (green line) contamination from reflections in the dish. The residuals of these foregrounds, cleaned to  $5\sigma$  after 2 minutes of integration, are plotted with (red dashed line) and without (cyan dashed line) dish reflections. We compare to the amplitude of the 21 cm power spectrum (solid black line). Foreground contamination, leaked by reflections, extends out to  $k_{\parallel} \approx 0.25 h\text{Mpc}^{-1}$ . The signals plummet to zero at  $k = 0$  is an artifact of the spatial extent of the simulation which does not probe extremely fine scales.

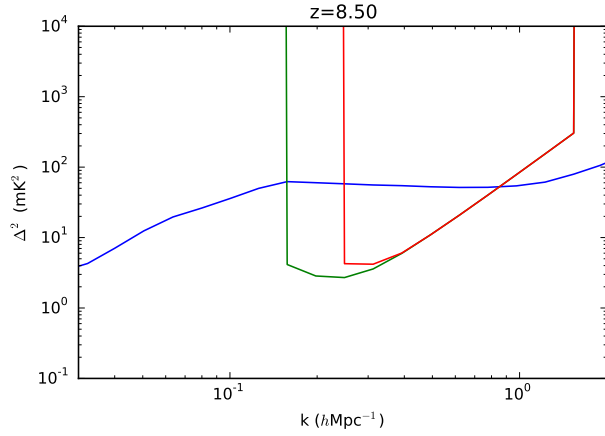


FIG. 10.— Comparison between sensitivities with and without reflections.

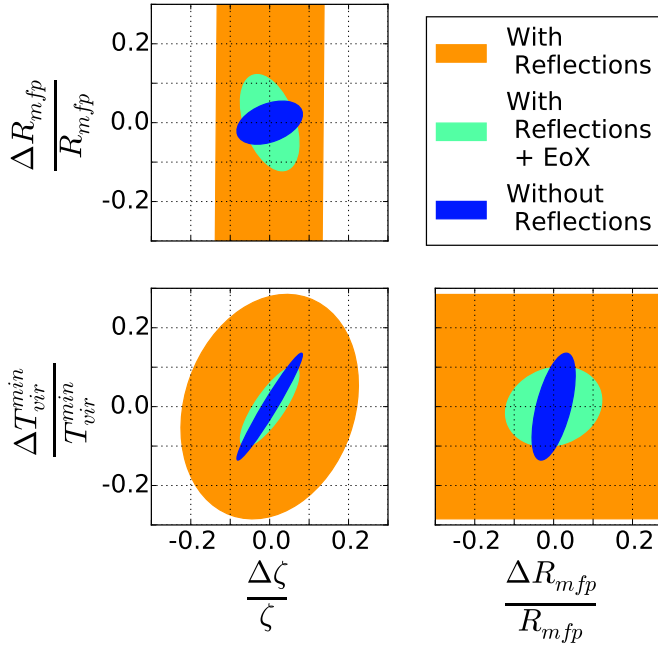


FIG. 11.— 95% confidence intervals with and without reflections. The primary effect of a large minimal delay accessible is that the “knee” which is the primary lever on  $R_{\text{mfp}}$  becomes inaccessible at low redshift. Since the comoving minimal  $k$  corresponding to a minimal delay becomes smaller at higher redshift, EoX measurements do improve constraints on  $R_{\text{mfp}}$ .

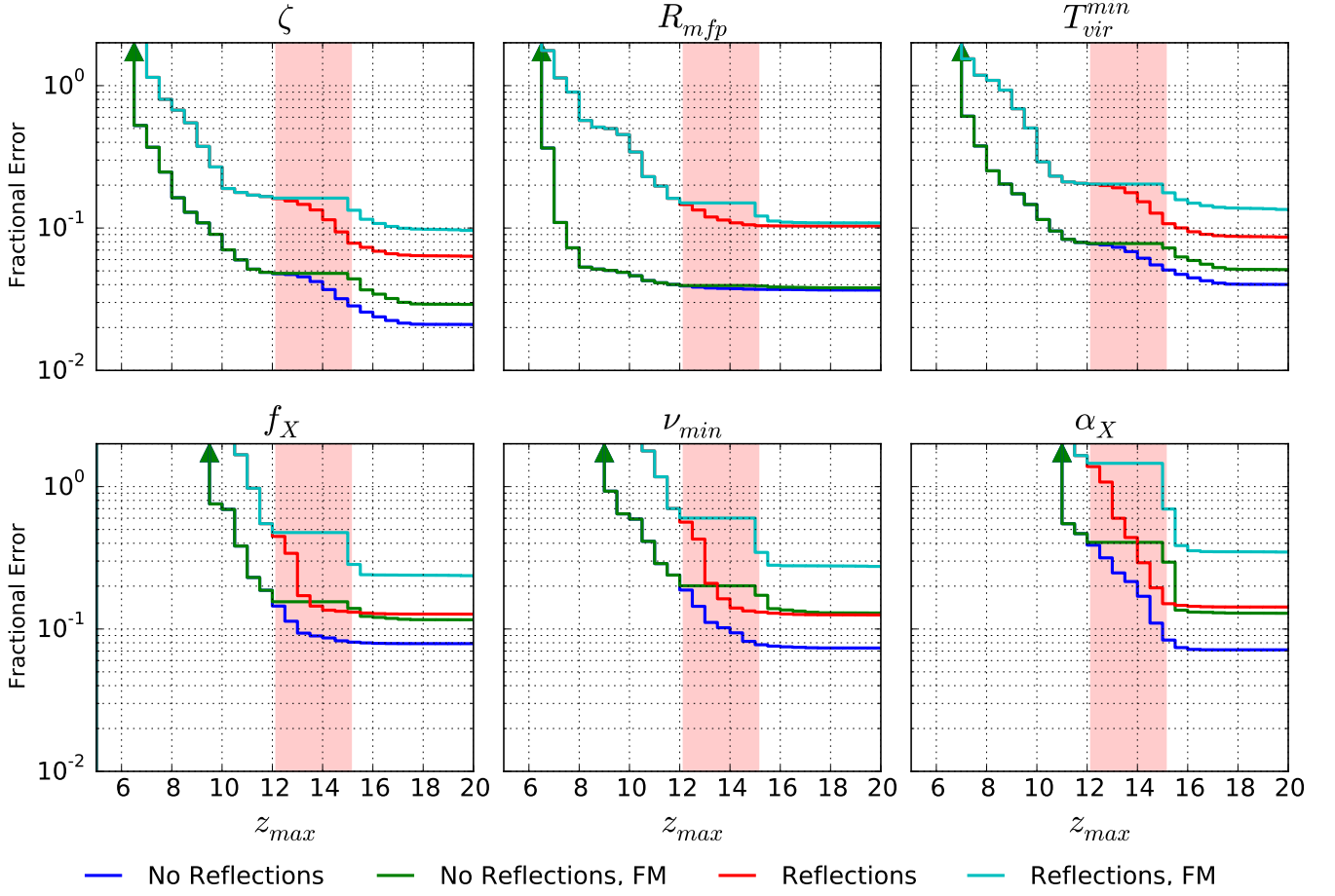


FIG. 12.— Fractional Errors on reionization and heating parameters as a function of maximal observed redshift.

Bowman, J. D., & Rogers, A. E. E. 2010, *Nature*, 468, 796  
 Burns, J. O., et al. 2012, *Advances in Space Research*, 49, 433  
 Datta, A., Bowman, J. D., & Carilli, C. L. 2010, *ApJ*, 724, 526  
 Dillon, J. S., et al. 2015, *Phys. Rev. D*, 91, 123011  
 Ewall-Wice, A., et al. submitted 2015, Submitted to MNRAS  
 Furlanetto, S. R., Oh, S. P., & Briggs, F. H. 2006, *Phys. Rep.*, 433, 181  
 Greenhill, L. J., & Bernardi, G. 2012, *ArXiv e-prints*  
 Liu, A., Parsons, A. R., & Trott, C. M. 2014a, *Phys. Rev. D*, 90, 023018  
 —. 2014b, *Phys. Rev. D*, 90, 023019  
 Liu, A., & Tegmark, M. 2011, *Phys. Rev. D*, 83, 103006  
 Morales, M. F., & Hewitt, J. 2004, *ApJ*, 615, 7  
 Morales, M. F., & Wyithe, J. S. B. 2010, *ARA&A*, 48, 127  
 Neben et al. submitted, *ApJ*  
 Paciga, G., et al. 2013, *MNRAS*, 433, 639  
 Parsons, A. R., Pober, J. C., Aguirre, J. E., Carilli, C. L., Jacobs, D. C., & Moore, D. F. 2012, *ApJ*, 756, 165

Parsons, A. R., et al. 2010, *AJ*, 139, 1468  
 Patra et al. submitted, *ApJ*  
 Pober, J. C., et al. 2014, *ApJ*, 782, 66  
 Pritchard, J. R., & Loeb, A. 2012, *Reports on Progress in Physics*, 75, 086901  
 Sokolowski, M., et al. 2015, *PASA*, 32, 4  
 Thyagarajan, N., et al. 2013, *ApJ*, 776, 6  
 —. 2015a, *ApJ*, 807, L28  
 —. 2015b, *ApJ*, 804, 14  
 Thyagarajan et al. submitted, *ApJ*  
 van Haarlem, M. P., et al. 2013, *A&A*, 556, A2  
 Vedantham, H., Udaya Shankar, N., & Subrahmanyan, R. 2012, *ApJ*, 745, 176  
 Voytek, T. C., Natarajan, A., Jáuregui García, J. M., Peterson, J. B., & López-Cruz, O. 2014, *ApJ*, 782, L9  
 Wieringa, M. H. 1992, *Experimental Astronomy*, 2, 203  
 Zheng, H., et al. 2014, *MNRAS*, 445, 1084

## APPENDIX

### THE EFFECT OF REFLECTIONS AND CROSS-TALK ON VISIBILITIES

In this section, we investigate, formally, the impact of reflections of electromagnetic waves between antennas and within the signal chain of single antennas on foreground leakage in 21 cm experiments. We start with the time varying electric field from a single source with location  $\mathbf{k}$  on the sky, arriving at antenna  $i$  with delay  $\tau_i$  and antenna  $j$  with delay  $\tau_j$  with respect to the electric field at the origin which we denote as  $s(t, \hat{\mathbf{s}})$ . We allow for two different types of reflections: First, we allow reflections within the analogue path of each  $i^{th}$  antenna which we denote as  $r_i(\tau, \hat{\mathbf{s}})$ . We also allow for single reflections between any  $i - j$  antenna pair which we denote as  $r_{ij}(\tau', \hat{\mathbf{s}})$ . Our choice of arbitrary  $\tau'$ , for now, allows for multi-path propagation between antennas, though we expect it to be dominated by the geometrical delay between the antenna pair. The electric field at antenna  $i$  is given by

$$s_i(t, \hat{\mathbf{s}}) = \int d\tau' r_i(\tau', \hat{\mathbf{s}}) s(t + \tau_i - \tau') + \sum_{j \neq i} \int d\tau' s(t + \tau_j - \tau_{ij}) r_{ij}(\tau', \hat{\mathbf{s}}) \quad (\text{A1})$$

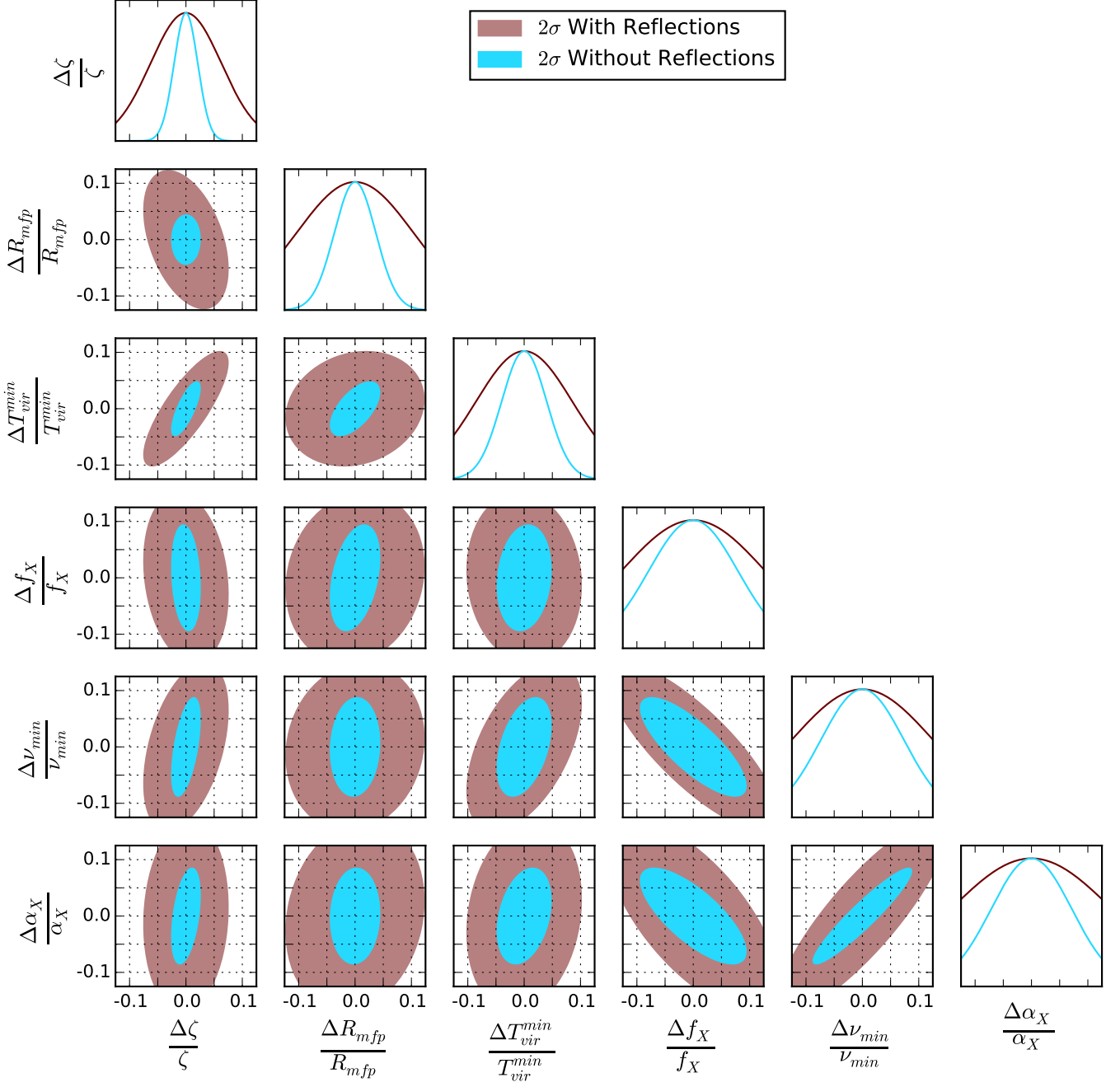


FIG. 13.— 95% confidence regions with and without reflections assuming that observations are taken over the redshifts between 5 and 25 are observed.

In an FX correlator, the electric field is sampled, Fourier transformed, and cross multiplied between antenna pairs to form visibilities. The Fourier transform step leaves us with

$$\tilde{s}_i(f, \hat{\mathbf{s}}) = \tilde{s}(f, \hat{\mathbf{s}}) \left[ \int d\tau' r_i(\tau', \hat{\mathbf{s}}) e^{2\pi i(\tau_i - \tau')f} + \sum_{j \neq i} \int d\tau' e^{2\pi i(\tau_j - \tau_{ij})f} r_{ij}(\tau', \hat{\mathbf{s}}) \right] \quad (\text{A2})$$

Multiplying and averaging gives us the visibility for the single source we obtain

$$\begin{aligned}
v'_{ij}(f, \hat{\mathbf{s}}) &= \langle \tilde{s}_i(f, \hat{\mathbf{k}}) \tilde{s}_j(f, \hat{\mathbf{s}}) \rangle_t \\
&= d\Omega I(f, \hat{\mathbf{s}}) g_i(f) g_j^*(f) a_i(f, \hat{\mathbf{s}}) a_j^*(f, \hat{\mathbf{s}}) e^{2\pi i \mathbf{u}_{ij} \cdot \hat{\mathbf{s}}} + d\Omega I(f, \hat{\mathbf{s}}) \sum_{\ell \neq j} g_i(f) a_i(f, \hat{\mathbf{s}}) C_{\ell j}^*(f, \hat{\mathbf{s}}) e^{2\pi i \mathbf{u}_{\ell i} \cdot \hat{\mathbf{s}}} \\
&\quad + d\Omega I(f, \hat{\mathbf{s}}) \sum_{k \neq i} g_j^*(f) a_j^*(f) C_{ki}(f, \hat{\mathbf{s}}) e^{2\pi i \mathbf{u}_{kj} \cdot \hat{\mathbf{s}}} + d\Omega I(f, \hat{\mathbf{s}}) \sum_{k \neq i} \sum_{\ell \neq j} C_{ki}(f, \hat{\mathbf{s}}) C_{j\ell}^*(f, \hat{\mathbf{s}}) e^{2\pi i \mathbf{u}_{k\ell} \cdot \hat{\mathbf{s}}}, \quad (\text{A3})
\end{aligned}$$

where  $g_i(f) a_i(f, \hat{\mathbf{s}}) = \int d\tau r_i(\tau, \hat{\mathbf{s}}) e^{2\pi i f \tau}$  is the effective direction dependent gain of the system which can be factored into a direction dependent and direction independent function where  $g_i(f)$  is the gain of the analogue signal chain after the radiation has been absorbed by the feed and  $a_i(f, \hat{\mathbf{s}})$  describes the chromatic electric field response of the antenna. The first term in equation A3 is an effective visibility with self-reflections. The two cross terms and the last term involve the mixing of visibilities complementary to the  $ij$  baseline and have the potential to introduce significant chromatic features since they potentially insert visibilities on much longer baseline lengths. Assuming propagation along a single path directly between the antennas, we may write  $C_{ik}(f, \hat{\mathbf{s}})$  as

$$C_{ki}(f, \hat{\mathbf{s}}) = a_i(f, \hat{\mathbf{s}}_{ik}) \frac{1}{r_{ik}} \left[ \frac{d\sigma_k}{d\Omega}(f, \hat{\mathbf{s}}, \hat{\mathbf{s}}_{ik}) \right]^{1/2} e^{2\pi i \tau_{ik} f} \quad (\text{A4})$$

Where  $r_{ik}$  is the distance between antennas  $i$  and  $k$ ,  $d\sigma_k(f, \hat{\mathbf{s}}, \hat{\mathbf{s}}_{ik})/d\Omega$  is the cross-section of the antenna to scatter radiation from the  $\hat{\mathbf{s}}$  direction to the  $\hat{\mathbf{s}}_{ik}$  direction where  $\hat{\mathbf{s}}_{ik}$  is the unit vector in the direction between antenna  $i$  and antenna  $k$ . Integrating over the primary beam, we obtain a full expression on the effect of the foregrounds.

$$\begin{aligned}
V'_{ij} &= \int d\Omega v'_{ij}(f, \hat{\mathbf{s}}) = g_i(f) g_j^*(f) \int d\Omega A_{ij}(f, \hat{\mathbf{s}}) I(f, \hat{\mathbf{s}}) e^{2\pi i f \mathbf{u}_{ij} \cdot \hat{\mathbf{s}}} + g_i(f) \sum_{\ell \neq j} \int d\Omega A_{i\ell j}(f, \hat{\mathbf{s}}) I(f, \hat{\mathbf{s}}) e^{2\pi i \mathbf{u}_{\ell i} \cdot \hat{\mathbf{s}}} \\
&\quad + g_j^*(f) \sum_{k \neq i} \int d\Omega A_{jki}^*(f, \hat{\mathbf{s}}) I(\hat{\mathbf{s}}, f) e^{2\pi i \mathbf{u}_{kj} \cdot \hat{\mathbf{s}}} + \sum_{k \neq i} \sum_{\ell \neq j} \int d\Omega A_{kilj}(f, \hat{\mathbf{s}}) I(f, \hat{\mathbf{s}}) e^{2\pi i \mathbf{u}_{k\ell} \cdot \hat{\mathbf{s}}} \quad (\text{A5})
\end{aligned}$$

which is essentially an ad-mixture of many baselines with different effective primary beams. We denote the effective primary beam of the  $i, j$  antenna pair as  $A_{ij}(f, \hat{\mathbf{s}}) = a_i(f, \hat{\mathbf{s}}) a_j^*(f, \hat{\mathbf{s}})$ , the effective beam from a single reflection correlated with a direct measurement as  $A_{i\ell j} = a_i(f, \hat{\mathbf{s}}) C_{\ell j}^*(f, \hat{\mathbf{s}})$  and the correlation between entirely reflected terms as experiencing an effective primary beam of  $A_{kilj} = C_{ki}(f, \hat{\mathbf{s}}) C_{j\ell}^*(f, \hat{\mathbf{s}})$ . In this paper, we focus on the reflection terms within a single antenna element. Hence, we ignore all but the first term for now. Any reflection terms occurring downstream of the conversion by the feed from electromagnetic radiation to voltage are lumped into  $g_i(f)$  and reflections occurring within the antenna element enter into  $a_i(f, \hat{\mathbf{s}})$ . While reflections within the analogue system are a potential source of contamination, HERA's post-feed analogue signal path is designed to keep all reflections under 35 m, within the wedge.

The focus of this paper and its companions is the reflection properties of the primary antenna element, so we will focus the rest of our discussion here on  $a_i(f, \hat{\mathbf{s}})$ . The primary elements of our dish include a feed and backplane suspended over a fourteen meter dish. We assume a set of discrete reflections within the dish, which without loss of generality are assumed to have frequency independent reflection coefficients<sup>8</sup> hence

$$a_i(f, \hat{\mathbf{s}}) = \sum_n r_n(\hat{\mathbf{s}}) e^{2\pi i \tau_n f} \quad (\text{A6})$$

Assuming all antennas are identical, we have

$$A_{ij}(f, \hat{\mathbf{s}}) = \sum_m \sum_n r_n(\hat{\mathbf{s}}) r_m^*(\hat{\mathbf{s}}) e^{2\pi i (\tau_n - \tau_m) f} = \sum_\alpha A_\alpha(\hat{\mathbf{s}}) e^{2\pi i \tau_\alpha f} \quad (\text{A7})$$

where we have re-indexed  $m$  and  $n$  under a single greek index  $\alpha$  in the second equality. The effect of internal reflections on a visibility is hence

$$V'_{ij} = \sum_\alpha \int d\Omega A_\alpha(\hat{\mathbf{s}}) e^{2\pi i \tau_\alpha f} e^{2\pi i \mathbf{b}_{ij} \cdot \hat{\mathbf{s}} f / c} I(f, \hat{\mathbf{s}}) \quad (\text{A8})$$

Taking the delay transform, one obtains

$$\tilde{V}'_{ij}(\tau) = \sum_\alpha \tilde{V}_{ij}^\alpha(\tau - \tau_\alpha) \quad (\text{A9})$$

where

$$\tilde{V}_{ij}^\alpha(\tau) = \int d\tau e^{-2\pi i f \tau} \int d\Omega A_\alpha(\hat{\mathbf{s}}) e^{2\pi i \mathbf{b}_{ij} \cdot \hat{\mathbf{s}} f / c} I(f, \hat{\mathbf{s}}) \quad (\text{A10})$$

<sup>8</sup> If we allow each coefficient to be frequency dependent, we can expand each frequency dependent term in a Fourier series of frequency independent terms

is the usual delay transform of Parsons et al. (2012).  $\tilde{V}_{ij}^{alpha}(\tau)$ .